Special Feature: Materials Analysis Using Quantum Beams

Key Technologies of Toyota Beamline at SPring-8: Quick-scanning X-ray Absorption Spectroscopy and Scanning Three-dimensional X-ray Diffraction Microscopy

Takamasa Nonaka, Yujiro Hayashi and Kazuhiko Dohmae

■ABSTRACT‖ We have developed two novel analytical techniques and installed these techniques at Toyota beamline (BL33XU) at SPring-8. One technique is a quick-scanning X-ray absorption fine structure (QXAFS) system, and the other is a scanning three-dimensional X-ray diffraction (3DXRD) system. Rapid acquisition of high-quality QXAFS data was realized by combining a servo-motor-driven Si channel-cut monochromator with a tapered undulator. Two tandemly arranged monochromators with channel-cut Si(111) and Si(220) crystals cover energy ranges of 4.0 to 28.2 keV and 6.6 to 46.0 keV, respectively. The QXAFS system allows users to instantly adjust scan parameters such as energy ranges and frequencies. Performance tests at the Cu K-edge demonstrated sufficiently high data quality for X-ray absorption near-edge structure (XANES) and extended X-ray absorption fine-structure (EXAFS) analyses with temporal resolutions of up to 10 and 25 ms, respectively. A modified three-dimensional X-ray diffraction method is proposed as a solution of the main problem of 3DXRD, i.e., polycrystalline diffraction spot overlap, which often occurs in the case of engineering materials such as steel. As a first demonstration, in situ three-dimensional crystallographic orientation mapping was performed for a plastically deformed coarse-grained iron sample using a 20-μm incident beam. The observed crystallographic rotation behaviors were reproduced by a crystal plasticity finite element model.

■KEYWORDS‖ Synchrotron Radiation, Tapered Undulator, Monochromator, XAFS, QXAFS, Scanning 3DXRD, 3D Orientation Mapping

1. Introduction

Toyota beamline (BL33XU) is a multi-purpose beamline at SPring-8, which was designed and constructed in collaboration with the Japan Synchrotron Radiation Research Institute (JASRI) and RIKEN.[1] The beamline is intended for use in studying a wide variety of materials for sustainable vehicle technology, such as auto exhaust catalysts, secondary batteries, fuel cells, and structural materials. Since commencing operation in 2009, studies using various analytical techniques, such as X-ray absorption spectroscopy, X-ray diffraction, small-angle X-ray scattering, and three-dimensional X-ray diffraction (3DXRD) microscopy have been actively performed.

Among these techniques, two unique techniques that characterize Toyota beamline are described in the present paper. One is time-resolved quick-scanning X-ray absorption spectroscopy, and the other is scanning three-dimensional X-ray diffraction microscopy. The design of the quick-scanning X-ray absorption fine structure (QXAFS) system and the results of performance tests conducted at Toyota beamline are presented in Section 2. The methodology of scanning 3DXRD and the results of the demonstration are described in Section 3.

2. QXAFS System with Servo-motor-driven Channel-cut Monochromator

Time-resolved QXAFS is a powerful tool for investigating in situ the dynamics of physical/chemical reactions that occur over time scales of seconds or shorter. Especially in studies of functional materials, which are the primary targets of Toyota beamline, in situ time-resolved measurements are essential for determining the mechanisms that give rise to their functions.[2-4] Various types of QXAFS techniques have been developed over the last two decades.[5-14] Frahm et al. acquired extended X-ray absorption fine
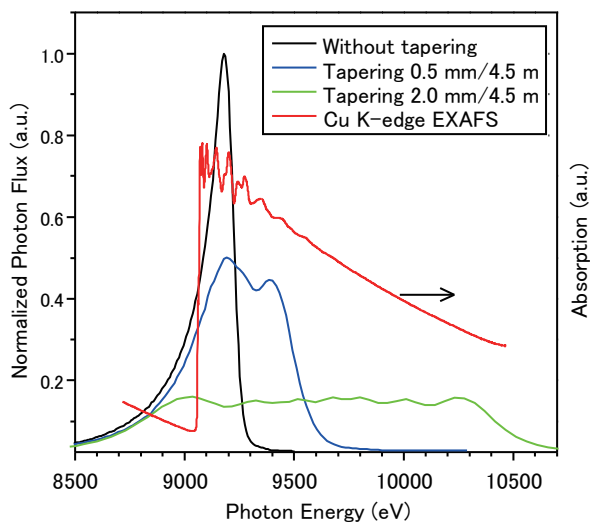
structure (EXAFS) spectra with a repetition rate of up to 40 Hz (i.e., temporal resolution: 12.5 ms) using a cam-driven monochromator.[9] Uruga et al. measured EXAFS spectra with a repetition rate of 10 Hz (50 ms) using a compact Si channel-cut crystal and quasi-monochromatic helical undulator radiation over an energy range of 8 to 17 keV.[11]

In order to realize XAFS measurements with shorter scanning time and a wider energy range, we developed a novel QXAFS system that uses a tapered undulator and a compact monochromator.[15] The tapered undulator provides a variable energy bandwidth as well as a high brilliance X-ray beam, while the compact monochromator allows for high-speed energy scanning with a servo-motor-driven channel-cut crystal.

2. 1 Instrumentation for the QXAFS System

2. 1. 1 Light Source and Optics

The light source of Toyota beamline is a tapered in-vacuum undulator, which is the first tapered undulator installed in SPring-8. The energy width is controllable by varying the taper ratio of the undulator gap. In tapering mode, the gaps on the exit side are wider than those on the entrance side. **Figure 1** shows the spectral fluxes of the undulator for different taper ratios with an average gap width of 14 mm. A Cu K-edge XAFS

spectrum of a Cu foil obtained with 2.0 mm/4.5 m tapering is also shown in the figure. The measured energy widths were 600 and 1700 eV for taper ratios of 0.5 mm/4.5 m and 2.0 mm/4.5 m, respectively, which are suitable for X-ray absorption near-edge structure (XANES) and EXAFS measurements. For XAFS measurements, higher harmonics are rejected using two 1000-mm-long upstream mirrors and two 700-mm-long downstream mirrors. All mirrors are coated with stripes of Pt and Rh and are bendable to focus the X-ray beam in the horizontal and vertical directions. The focused beam size was measured to be approximately 200 μm × 900 μm (H × W) (full width at half maximum), and the total photon flux was estimated to be approximately 10^{13} photons/s at 12 keV.

2. 1. 2 Monochromator

The key components of our QXAFS monochromator are the direct-drive servo motor and the compact channel-cut crystal. The maximum oscillation frequency of the crystal, which determines the minimum temporal resolution, depends on the inertia of the crystal and the holders and on the torque of the servo motor. The Si channel-cut crystal was designed to be compact in order to reduce the rotational inertia of high-frequency mechanical oscillations (**Fig. 2**). The crystal has a narrow 3-mm-wide gap between the reflecting planes, which enables the crystal to be downsized to 70 mm × 70 mm × 70 mm. The crystal shape allows double-bounce Bragg reflection over an angular range of 4° to 30°. The reflecting planes
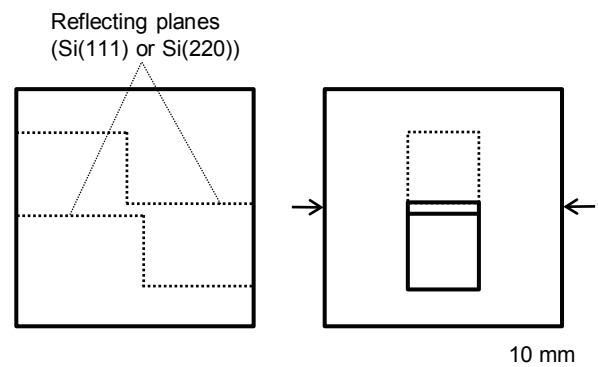

Fig. 1   Measured on-axis spectral flux of the fundamental harmonic of the tapered in-vacuum undulator (average gap width: 14 mm) and a Cu K-edge XAFS spectrum of a Cu foil obtained with 2.0 mm/4.5 m tapering.

Fig. 2   Schematic diagram of Si channel-cut crystal (left: side view; right: view from downstream). Arrows indicate surfaces that contact the liquid-nitrogen-cooled Cu blocks.

were fabricated inside the crystal by hollowing out the single-crystal silicon block. The first and second reflecting planes are arranged to be geometrically equivalent so that they are uniformly cooled, which results in a reduction in the throughput loss.

A schematic diagram of the interior of the monochromator is shown in **Fig. 3**. The channel-cut crystal is clamped on both sides by liquid-nitrogen-cooled copper blocks. This arrangement enables the crystal to be tightly held in order to withstand high-frequency oscillation and reduces deformation of the reflecting plane owing to the clamping force. For better thermal contact, 0.5-mm-thick indium sheets are inserted at the interface between the crystal and the copper blocks.

The heat load on the crystal was estimated to be approximately 60 W using the synchrotron radiation calculation code SPECTRA.[16] Subsequently, the slope error of the reflecting plane due to thermal deformation was calculated to be less than 5 μrad using the ANSYS code, which is sufficiently small to maintain double-bounce Bragg conditions.

The crystal holder is rotated by a high-precision, high-torque AC direct-drive servo motor (Nikki Denso, D250-100-F), which is installed outside the vacuum vessel. A magnetic fluid rotary feedthrough seal unit (Rigaku Mechatronics) transfers the rotary motion of the servo motor to the crystal holder inside the vacuum vessel. The motor has a maximum torque of 186 Nm, a rated torque of 62 Nm, and a rated power of

1200 W. The angular resolution of the monochromator is 10^{-4} degrees (0.36 arcsec), which is determined by the resolution of the servo-motor internal encoder.

Two monochromators are arranged in tandem in the first experimental hutch of Toyota beamline.[1] The monochromators with Si(111) or Si(220) crystals cover energy ranges of 4.0 to 28.2 keV and 6.6 to 46.0 keV, respectively. The two monochromators can be interchanged on the X-ray beam axis using vertical translation stages without breaking the vacuum in the vessels. The height of the X-ray beam that exits from the monochromator varies slightly during QXAFS scans (up to 220 μm during a scan from 4.0 to 5.5 keV). However, the downstream vertical focusing mirrors can maintain the beam height at the sample position.

2. 1. 3 Control and Measurement System

We constructed a control system for three XAFS scanning modes with different time resolutions. **Table 1** shows the specifications of these three scanning modes. For the continuous scanning mode, the undulator gap is tapered and the angular velocity of the servo motor has a triangular wave profile. However, for scanning faster than 0.5 Hz (i.e., temporal resolution of less than 1 s), the servo motor cannot oscillate with a triangular wave due to the inertia of the crystal and the holder. Rather, the servo motor oscillates with a sinusoidal wave (termed the super quick scan mode). For XAFS scans that require longer measurement times, the servo motor rotates incrementally and the undulator gap is not tapered. Rather, the servo motor is tuned to maximize the photon flux at each measurement point (step scan mode). These three scan modes can be
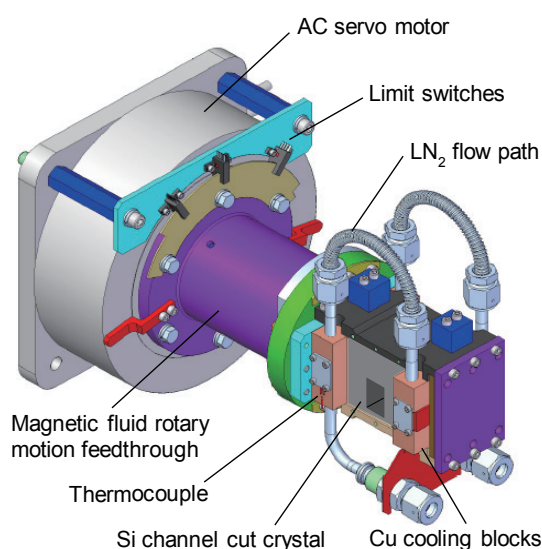
Fig. 3　Schematic of interior of the direct-drive servo-motor driven monochromator.
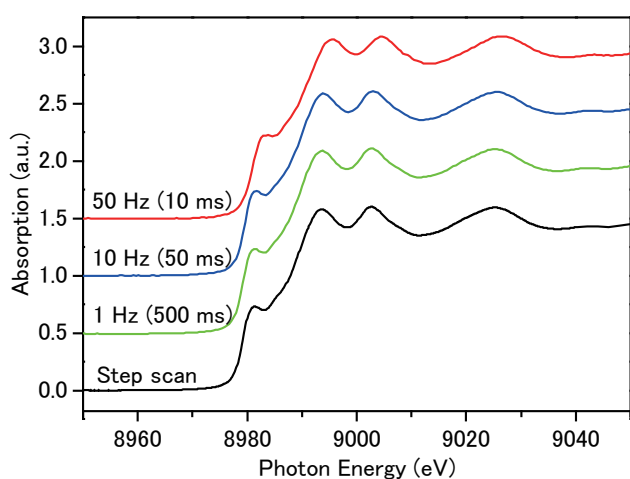
Table 1　Specifications of three XAFS scanning modes available with the system.

Mode	Super quick scan	Continuous scan	Step scan
Temporal resolution	< 1 s	1 s -1 min.	>1 min.
Motion pattern	Sinusoidal wave	Triangular wave	Incremental
Undulator gap	Tapered	Tapered	Non-tapered
Data acquisition	ADC	Counter /ADC	Counter

switched in a very short time, and the scan parameters (energy ranges, starting angles of oscillations, and frequencies) can be adjusted instantly. The control and measurement system is fully operated by a PC using application software written in LabVIEW.

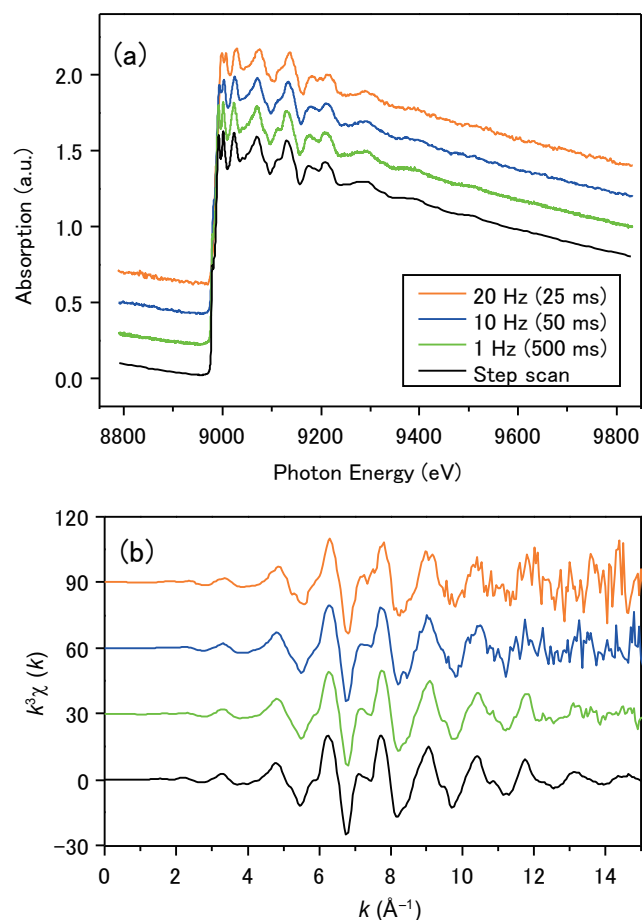## 2. 2　Performance of the QXAFS System

Performance tests in the super quick scan mode were conducted at Toyota beamline in order to characterize our QXAFS system. **Figure 4** shows XANES spectra for a Cu foil measured at different scan speeds with an angular range of 0.2° using the Si(111) monochromator. Each scan was performed from the lowest to the highest energy. The spectra were extracted from the entire cyclic-scan data and were then plotted. The undulator gap had a taper ratio of 0.5 mm/4.5 m. The pre-edge peak around 8980 eV, which is representative of metallic Cu, is clearly visible even in the 50-Hz oscillation spectrum. The signal-to-noise ratio of the 50-Hz oscillation spectrum is sufficiently high for analysis due to the high incident X-ray flux from the tapered undulator and to the low-noise data acquisition system. This indicates that our QXAFS system (including the light source, beamline optics, and measurement system) operates effectively with a temporal resolution of up to 10 ms. However, compared to the step scan spectra, slight spectral distortions and shifts to higher energies

are observed, particularly in the faster scan spectrum. These deviations originate from the response delay of the ionization chambers, which was estimated to be several tens of microseconds. Overcoming this problem should be possible by using detectors with faster responses.

Figure 5 shows $\mu(E)$- and k^3-weighted $\chi(k)$-EXAFS spectra for a Cu foil measured with an angular range of 2.0°. The taper ratio of the undulator gap was 2.0 mm/4.5 m. The data quality of the super quick scan spectra was slightly worse than that of the step scan spectrum measured over approximately 20 min due to the difference in their measurement times. However, meaningful EXAFS spectra were obtained for $k < 12$ Å^{-1}, even from 20-Hz oscillation spectrum, demonstrating that the super quick scan mode of our QXAFS system is also effective for EXAFS measurements.

Fig. 4　Cu K-edge XANES spectra of 6-μm-thick Cu foil measured in super quick scan mode using the Si(111) channel-cut crystal (undulator gap taper: 0.5 mm/4.5 m). A step scan spectrum is also shown for comparison.

Fig. 5　(a) Cu K-edge $\mu(E)$- and (b) k^3-weighted $\chi(k)$-EXAFS spectra of Cu foil measured in super quick scan mode (undulator gap taper: 2.0 mm/4.5 m).

2. 3 Summary

We developed a novel QXAFS system using a servo-motor-driven compact crystal monochromator and installed in a tapered undulator beamline, Toyota beamline, at SPring-8. The system can obtain XAFS spectra in tens of milliseconds over a wide energy range of 4.0 to 46.0 keV using Si(111) and Si(220) monochromators. Performance tests at Cu K-edge demonstrated that our QXAFS system has a satisfactory temporal resolution, energy range, and data quality, as well as satisfactory flexibility of the control system. This system is now playing an essential role at Toyota beamline in investigating the dynamics of chemical reactions of functional materials by time-resolved in situ QXAFS measurements.

3. Scanning Three-dimensional X-ray Diffraction Microscopy

Toward further optimization of commercial product design with engineering materials such as steel and light alloys, the development of computational material models is needed because traditional materials development methodologies are too expensive and time consuming. Constitutive models based on crystal plasticity provide a more accurate prediction of local deformation than Hill's self-consistent method.[17] Nevertheless, the use of information from such models in the design process is still risky for design engineers due to a lack of appropriate experimental data and methods to validate such models.

At present, the most widely used experimental methodology for the validation of such models for engineering metals and alloys is crystallographic orientation imaging microscopy (OIM) by the electron backscatter diffraction (EBSD) technique. In the EBSD technique, the orientation is mapped point by point on the surface. Successive serial sectioning of samples allows us to obtain three-dimensional (3D) voxel-by-voxel orientation maps. However, we cannot track deformation because mapped volumes are destroyed.

Recently, a third-generation synchrotron-based X-ray diffraction technique has enabled new methods to be used. High-energy diffraction approaches based on 3D X-ray diffraction microscopy (3DXRD) enable the non-destructive 3D mapping of orientation and stress in metals and alloys.[18-20] The main problem in 3DXRD-type experiments is that polycrystalline diffraction spots overlap on area detectors. Engineering metals and alloys, such as steel, tend to cause diffraction spots to overlap due to, for example, (i) a large number of grains, (ii) mosaicity, (iii) elastic and plastic strain, and (iv) texture.

In the present study, we propose a modified 3DXRD technique as a solution to the main problem. The modified method, referred to as scanning 3DXRD, achieves 3D orientation mapping using an incident beam that is sufficiently narrower than the average grain size. As a first demonstration, a 3D orientation mapping experiment using 20-μm slits for the incident beam was performed for a well-annealed coarse-grained polycrystalline iron sample.[21] The observed plastic deformation behaviors of ferrite grains were simulated using a crystal plasticity finite element (CPFE) model.[22]

3. 1 Experimental Setup and Data Acquisition

X-rays from the undulator without tapering at Toyota beamline are monochromatized to 35 to 60 keV using a stabilized liquid-nitrogen-cooled double Si(111) or Si(311) crystal monochromator. The monochromatic beam illuminates a polycrystalline sample through focusing optics or slits. The incident beam size is sufficiently smaller than the average grain size. The sample is mounted on an ω rotation stage with a rotation axis perpendicular to the incident beam. The ω rotation stage is mounted on X and Z translation stages in the $-x$ and z directions, respectively, where xyz is the laboratory coordinate system, as shown in **Fig. 6**. The diffraction from multiple grains is detected at a far-field area using an X-ray flat panel area detector. The diffraction patterns from multiple grains on the far-field area detector are assumed to be non-overlapping multiple spots. The diffraction images are continuously collected at a constant exposure time for ω values of 0° to 180° in steps of approximately 0.4°. The ω scans are conducted as X is translated in steps of ΔX. The ω-X scans are conducted as Z is translated in steps of ΔZ. The X and Z scan steps, ΔX and ΔZ, are chosen to be equal or similar to the incident beam width and height, respectively.

3. 2 Data Analysis
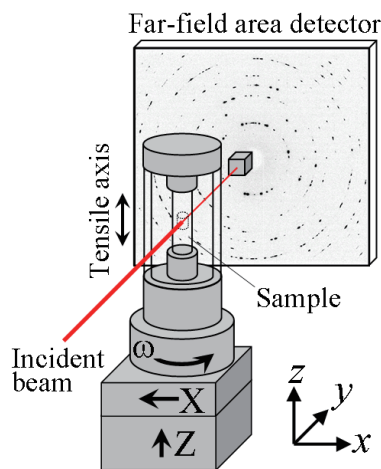
In the scanning 3DXRD analysis, the grain occupying

point (x_s, y_s, z_s) is determined, where x_s, y_s, and z_s are rectangular coordinates fixed to the sample. The point (x_s, y_s, z_s) is swept point by point in the field of view. Obviously, z_s is determined by z, where the incident beam illuminates the sample. Then, the problem is on the layer illuminated by an ω-X scan. First, the data set at (ω, X) satisfying the following relation:

$$X(\omega)/\Delta X = [\sqrt{x_s^2 + y_s^2} \cos(\omega + \tan^{-1}y_s/x_s)/\Delta X + 1/2]$$

is extracted from ω-X scan data, where [ ] is Gaussian notation. Multi-crystal indexing[23-27] is applied to the above diffraction image data set. The number of detected diffraction spots, N, for each grain is determined by the multi-crystal indexing. The grain with the highest N/M is assumed to occupy the point (x_s, y_s), where M is the theoretical maximum value of N, and depends on the orientation. Further refinements for the orientation and lattice parameters are performed by fitting the diffraction spot positions from the grain occupying (x_s, y_s). Then, the orientation and lattice parameters at (x_s, y_s) are determined. The spatial resolution is given by $2\Delta X$. The multi-crystal indexing and the refinements can be performed using "ImageD11"[28] in the suite of 3DXRD programs, "FABLE".[29]

3. 3 Demonstration

As a first demonstration, an experiment was conducted using vertical and horizontal slits with a 20-μm aperture to form a narrow incident beam. The X-ray photon energy was chosen to be 40 keV using the Si(220) compact monochromator. In order to prepare a coarse-grained iron sample with a grain size larger than the incident beam size, an iron wire having a purity of 99.5% and an outer diameter of 500 μm was annealed at 1250°C for 5 hours. The average grain size was estimated to be approximately 60 μm. The sample was mounted in an in situ tensile testing apparatus, which was mounted on the ω rotation stage. The 3D orientation mapping with $\Delta X = 25$ μm, a X scan range of ±100 μm, $\Delta Z = 25$ μm, and a Z scan range of ±75 μm was performed at a tensile strain $\varepsilon = 0.2\%$, 4.0%, 8.0%, and 10.7%. Although M depends on the grain orientation, it was approximated as a constant in the demonstration, which may cause errors in the orientation of about 10% of the voxels at grain boundaries.

The 3D orientation map at $\varepsilon = 0.2\%$ is shown in **Fig. 7**(a). Each grain and neighboring grains can be clearly distinguished according to the continuity and discontinuity of orientations in three dimensions, respectively. In order to evaluate the crystallographic


Fig. 6   Schematic diagram of scanning 3DXRD experimental setup.
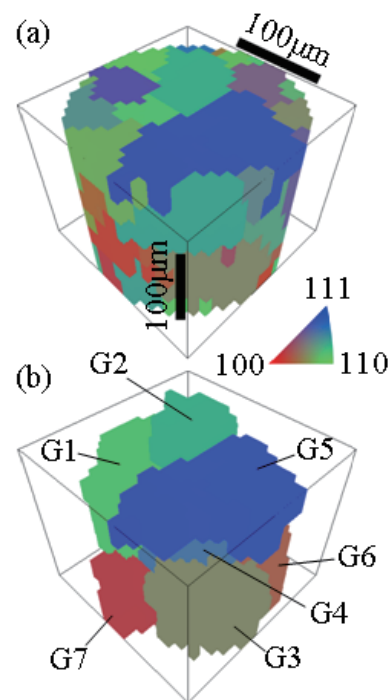
Fig. 7   Three-dimensional orientation map at $\varepsilon = 0.2\%$ (a) and extracted grains G1-G7 (b). The mapped volume and the voxel size are ϕ200 μm × 175 μm and 6.7 μm × 6.7 μm × 25 μm, respectively. The voxels are 25 μm long in the z direction. The colors correspond to the inverse pole figure for the tensile direction shown as a stereographic triangle.

rotation of each grain, some grains, G1-G7, were selected, as shown in Fig. 7(b). The 3D orientation maps at ε = 4.0%, 8.0%, and 10.7% are shown in **Figs. 8**(a) through 8(c). Grain boundaries become blurred as ε increases, while boundaries at ε = 0.2% are sharp. This blurring of boundaries is an artifact caused by the decrease of *N/M* at boundaries due to deformation. The orientations of all the voxels in G1-G7 at ε = 0.2% to 10.7% are plotted as an inverse pole figure for the tensile direction in **Fig. 9**(a). The plots at ε = 0.2% are concentrated approximately at single points, implying no significant intragranular misorientations. On average, the grains rotate approximately toward the <110> preferred orientation of the bcc uniaxial tensile texture. The orientation distribution of the grains expands as ε increases. This indicates that

intragranular misorientation occurs. Furthermore, significant intragranular multidimensional rotation is observed for G5 and G6. A small part of G5 with an orientation close to the <100> - <111> edge in the <111> corner of the stereographic triangle rotates toward <100>, whereas the average G5 rotates toward <110>. G6, whose orientation is near the <100> corner of the triangle, rotates uniformly toward orientations between <110> and <111>.

3. 4 Crystal Plasticity Finite Element Simulation

In order to verify the validity of the constitutive models based on crystal plasticity, experimentally mapped orientations before deformation are directly adopted as the initial orientation for finite elements.
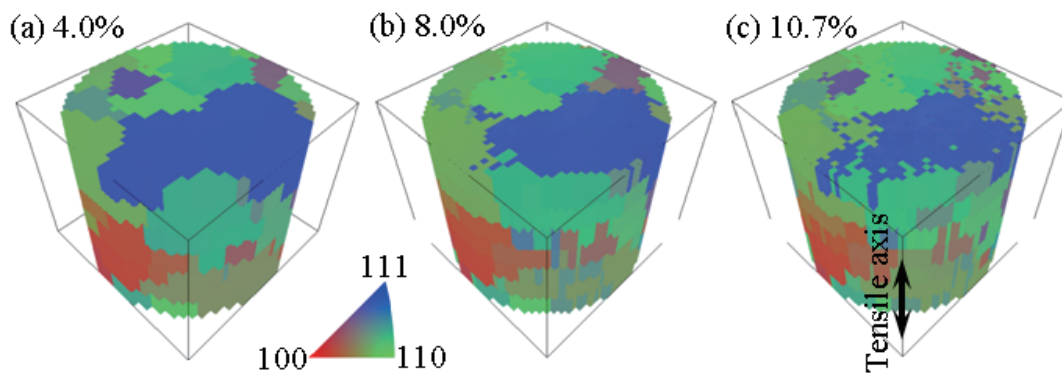
Fig. 8 Three-dimensional orientation maps at ε = 4.0% (a), 8.0% (b) and 10.7% (c). The voxel size is 5 μm × 5 μm × 25 μm in (a) and 4 μm × 4 μm × 25 μm in (b) and (c).
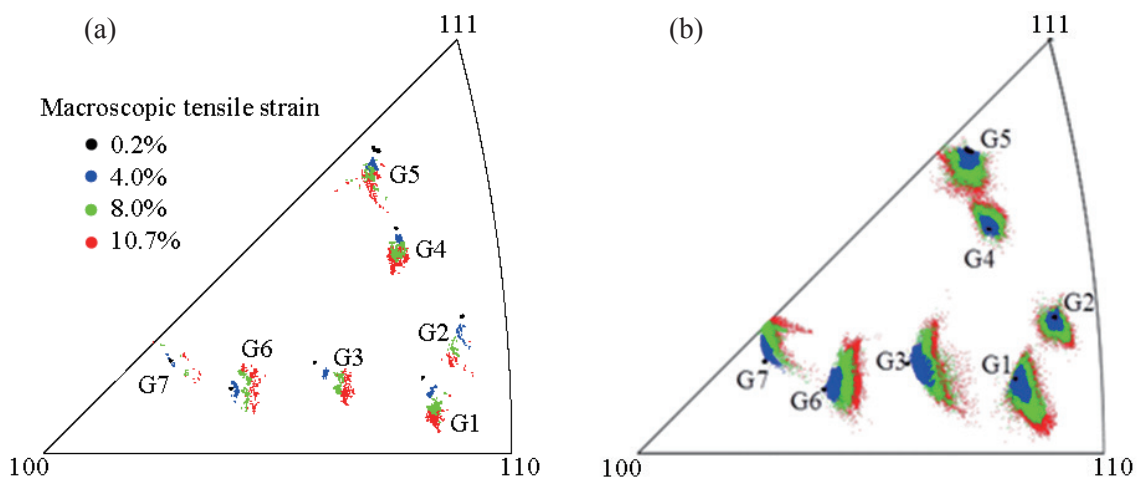
Fig. 9 Experimental (a) and simulated (b) inverse pole figures for the tensile direction for grains G1-G7 in a stereographic triangle at ε = 0.2%, 4.0%, 8.0% and 10.7%. All of the tensile directions for each voxel in G1-G7 are plotted for the different ε values.

Each experimental voxel is discretized by multiple standard isoparametric hexahedron finite elements. Each element is assigned to a single crystal or a single anisotropic elastic-plastic constituent. For ferritic crystal, 48 slip systems, {011}<111>, {112}<111>, and {123}<111>, are adopted, and the elastic stiffness is obtained from the literature. The constitutive equations and the adopted hardening law are reported elsewhere.[22,30] Other material constants are determined by reproducing experimental macroscopic stress-strain relationships. Elements out of the scanning 3DXRD experimental field of view are assigned to isotropic elastic-plastic elements. For boundaries formulated by the isotropic elastic-plastic elements, a periodic boundary condition is adopted.

The experimental results, i.e., the mean rotation toward the preferred orientation (except for the case of G4), the increase in intragranular misorientation, and the intragranular multidirectional rotations of G6, were reproduced by the CPFE simulation, as shown in Fig. 9(b). The simulated intragranular misorientations are larger than the experimental values because the experiment underestimates intragranular misorientations and the simulation overestimates them. In the latest simulation, the behavior of G4 and G5 has been reproduced taking into account the orientation dependence of M, and the other 36 slip systems involving {112}<111> and {123}<111>.

3. 5 Summary

We proposed a modified 3DXRD method, referred to as scanning 3DXRD, as a solution of the main problem of 3DXRD, i.e., polycrystalline diffraction spot overlap. As a first demonstration, an in situ 3D orientation mapping experiment was performed for a plastically-deformed polycrystalline iron sample with an average grain size of approximately 60 μm using a 20-μm incident beam. The observed significant crystallographic rotation behaviors are as follows: (i) mean rotations toward the bcc uniaxial tensile texture, (ii) increase in intragranular misorientation due to deformation, and (iii) intragranular multidirectional rotations. The observed rotation behaviors were simulated using a CPFE model in which the observed 3D orientation map before deformation was directly adopted as the initial orientation map. The rotation behaviors were reproduced through simulation, although the experiment underestimated intragranular

misorientations. Mapping with a higher spatial resolution is expected to provide more accurate estimation of the validity of models. For higher spatial resolution, a high-energy (50 keV) microbeam using 400-mm-long Pt-coated Kirkpatrick-Baez Si mirrors has been installed at Toyota beamline.

References

(1) Hirose, Y., *SPring-8 Res. Front. 2009* (2010), p. 170, JASRI.

(2) Tada, M. et al., *Angew. Chem. Int. Ed.*, Vol. 46 (2007), pp. 4310-4315.

(3) Yamamoto, T. et al., *Angew. Chem. Int. Ed.*, Vol. 46 (2007), pp. 9253-9256.

(4) Nagai, Y. et al., *Angew. Chem. Int. Ed.*, Vol. 47 (2008), pp. 9303-9306.

(5) Frahm, R., *Nucl. Instrum. Methods Phys. Res. A*, Vol. 270 (1988), pp. 578-581.

(6) Frahm, R., *Rev. Sci. Instrum.*, Vol. 60, No. 7 (1989), pp. 2515-2518.

(7) Richwin, M. et al., *J. Synchrotron Rad.*, Vol. 8 (2001), pp. 354-356.

(8) Richwin, M. et al., *Rev. Sci. Instrum.*, Vol. 73, No. 3 (2002), pp. 1668-1670.

(9) Frahm, R. et al., *Phys. Scr.*, Vol. T115 (2005), pp. 974-976.

(10) Caliebe, W. et al., *Radiat. Phys. Chem.*, Vol. 75 (2006), pp. 1962-1965.

(11) Uruga, T. et al., *AIP Conf. Proc.*, Vol. 882 (2007), pp. 914-916.

(12) Stötzel, J. et al., *Rev. Sci. Instrum.*, Vol. 79, No. 8 (2008), 083107.

(13) Khalid, S. et al., *Rev. Sci. Instrum.*, Vol. 81, No. 1 (2010), 015105.

(14) Stötzel, J. et al., *Rev. Sci. Instrum.*, Vol. 81, No. 7 (2010), 073109.

(15) Nonaka, T. et al., *Rev. Sci. Instrum.*, Vol. 83, No. 8 (2012), 083112.

(16) Tanaka, T. and Kitamura, H., *J. Synchrotron Rad.*, Vol. 8 (2001), pp. 1221-1228.

(17) Hill, R., *J. Mech. Phys. Solids*, Vol. 13 (1965), pp. 89-101.

(18) Poulsen, H. F., *Three-Dimensional X-ray Diffraction Microscopy* (2004), 156p., Springer.

(19) Poulsen, H. F., *Advanced Tomographic Methods in Mater. Sci. and Eng.* (2008), pp. 249-276, Oxford Univ. Press.

(20) Poulsen, H. F., *J. Appl. Cryst.*, Vol. 45 (2012), pp. 1084-1097.

(21) Hayashi, Y. et al., *Mater. Sci. Forum*, Vol. 777 (2014), pp. 118-123.

(22) Setoyama, D. et al., *Mater. Sci. Forum*, Vol. 777 (2014), pp. 142-147.

(23) Lauridsen, E. M. et al., *J. Appl. Cryst.*, Vol. 34 (2001), pp. 744-750.

(24) Ludwig, W. et al., *Rev. Sci. Instrum.*, Vol. 80 (2009), pp. 33905-33909.
(25) Moscicki, M. et al., *Mater. Sci. Eng. A*, Vol. 524 (2009), pp. 64-68.
(26) Oddershede, J. et al., *J. Appl. Cryst.*, Vol. 43 (2010), pp. 539-549.
(27) Bernier, J. V. et al., *J. Strain Analysis*, Vol. 46 (2011), pp. 527-554.
(28) Wright, J., "ImageD11", *FABLE*, <http://sourceforge.net/p/fable/wiki/imaged11/>, (accessed 2015-3-5).
(29) Sørensen, H. O. et al., *Z. Kristallogr.*, Vol. 227 (2012), pp. 63-78.
(30) Iwata, N. et al., *R&D Rev. Toyota CRDL*, Vol. 45, No. 4 (2014), pp. 1-10.

Figs. 1-5 and Table 1
Reprinted from Rev. Sci. Instrum., Vol. 83, No. 8 (2012), 083112, Nonaka, T., Dohmae, K., Araki, T., Hayashi, Y., Hirose, Y., Uruga, T., Yamazaki, H., Mochizuki, T., Tanida, H. and Goto, S., Quick-scanning X-ray Absorption Spectroscopy System with a Servo-motor-driven Channel-cut Monochromator with a Temporal Resolution of 10 ms, © 2012 AIP Publishing LLC, with permission from AIP Publishing LLC.

Figs. 6-9(a)
Reprinted and modified from Mater. Sci. Forum, Vol. 777 (2014), pp. 118-123, Hayashi, Y., Hirose, Y. and Setoyama D., In Situ Three-dimensional Orientation Mapping in Plastically-deformed Polycrystalline Iron by Three-dimensional X-ray Diffraction, © 2014 Trans Tech Publications Inc., with permission from Trans Tech Publications Inc.

Fig. 9(b)
Reprinted from Mater. Sci. Forum, Vol. 777 (2014), pp. 142-147, Setoyama, D., Hayashi, Y. and Iwata, N., Crystal Plasticity Finite Element Analysis based on Crystal Orientation Mapping with Three-dimensional X-ray Diffraction Microscopy, © 2014 Trans Tech Publications Inc., with permission from Trans Tech Publications Inc.

Takamasa Nonaka
  Research Field:
    - X-ray Absorption Spectroscopy
  Academic Degree: Dr.Eng.
  Academic Society:
    - The Japanese Society for Synchrotron Radiation Research
  Award:
    - Promotion Award from the Ceramic Society of Japan, 2008

Yujiro Hayashi
  Research Field:
    - Synchrotron-based X-ray Diffraction
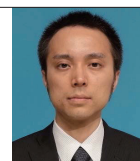 Academic Degree: Dr.Eng.
  Academic Societies:
    - The Japanese Society for Synchrotron Radiation Research
    - The Japan Institute of Metals and Materials
  Award:
    - Paper Award of the Japan Society of Applied Physics, 2010

Kazuhiko Dohmae
  Research Field:
    - X-ray Absorption Spectroscopy
  Academic Societies:
    - The Japanese Society for Synchrotron Radiation Research
    - Society of Automotive Engineers of Japan
    - The Surface Science Society of Japan
    - Catalysis Society of Japan
  Awards:
    - The Outstanding Technical Paper Award from Society of Automotive Engineers of Japan, 2004
    - The Catalysis Society of Japan Award, 2013